HOKKAIDO UNIVERSITY

Title	Pulsatory rise of microbubble swarm along a vertical wall
Author(s)	Kitagawa, Atsuhide; Murai, Yuichi
Citation	Chemical Engineering Science, 116, 694-703 https://doi.org/10.1016/j.ces.2014.06.001
Issue Date	2014-09-06
Doc URL	http://hdl.handle.net/2115/57102
Type	article (author version)
File Information	CES2014kitagawa.pdf

Instructions for use

Hokkaido University Collection of Scholarly and Academic Papers : HUSCAP

Pulsatory rise of microbubble swarm along a vertical wall

Atsuhide Kitagawa [a,*], Yuichi Murai [b]

[a] Department of Mechanical and System Engineering, Kyoto Institute of Technology, Goshokaido-cho, Matsugasaki, Sakyo-ku, Kyoto 606-8585 Japan

[b] Division of Energy and Environmental System, Faculty of Engineering, Hokkaido University, Kita-13, Nishi-8, Kita-ku, Sapporo 060-8628 Japan

* Corresponding author. Tel: +81 75 724 7327; Fax: +81 75 724 7300;
E-mail: kitagawa@kit.ac.jp (A. Kitagawa).

ABSTRACT

Based on the experimental finding that microbubble swarms dramatically promote heat transfer from a vertical heated wall, despite their potentially adiabatic nature, tests of microbubble fluid mechanics in the isothermal state are performed to clarify the unique motion characteristics of microbubble swarms. At constant bubble flow rate, the microbubble swarm shows a significant pulsatory rise along a vertical flat wall, particularly for small bubbles. Particle tracking velocimetry applied to the microbubbles shows that a two-way interaction between the microbubbles and the liquid flow self-excites the pulsation during their co-current rise. The sequence consists of the following processes: i) increase in the bubble number density close to the wall as a result of the liquid velocity gradient driven by the microbubbles themselves; ii) wave generation inside the microbubble swarm to induce the pulsatory rise of the swarm; and iii) amplification of the waves, which results in void-bursting motion in the final stage.

Keywords: Microbubble, Bubble swarm, Multiphase flow, Particle tracking velocimetry

1. Introduction

The influence of gas bubbles on heat transfer has long been an important topic in engineering. Studies on this subject are classified into boiling two-phase heat transfer (Dhir, 1998; Ivashnyov and Smirnov, 2004; Yang and Prosperetti, 2008; Legendre et al., 1998) and non-boiling two-phase heat transfer. Our study focuses on the latter, in which in most cases bubble motion close to a heated wall plays a critical role in modification of the heat transfer. For non-boiling two-phase heat transfer, Kenning and Kao (1972), Celata et al. (1999) and Tokuhiro and Lykoudis (1994) experimentally investigated forced convection two-phase heat transfer, mixed convection two-phase heat transfer and natural convection two-phase heat transfer, respectively, and found that the heat transfer coefficient was significantly enhanced by the injection of bubbles of a few mm in diameter. In this research, the heat transfer enhancement is a result of liquid velocity fluctuations induced by the wakes behind the individual bubbles and vortex shedding from the bubble interface, although the flow fields differ considerably among the three cases. Based on an analogy of heat transfer to mass and momentum transfer, Timkin and Gorelik (2009) showed the effects of sub-millimeter bubbles that rise along a vertical pipe wall, and deduced the heat

transfer enhancement from their wall friction data.

Currently, researchers are studying the effects of bubbles with diameters of less than 100 μm (i.e., microbubbles, Johnson and Cooke, 1981; Makuta et al., 2006; Dressaire et al., 2008; Suslov et al., 2012) on heat transfer, and expect a different effect from that of large bubbles (i.e., millimeter bubbles). The main questions over the use of such fine bubbles are the role of the high local number density of buoyant sources, and the effect of the interfacial tension that defines the rheological properties of the microbubble mixture (Llewellina and Manga, 2005). In particular, the microbubbles are kept tightly spherical by the dominance of the interfacial tension, and tend to produce repulsive forces during the collision of multiple bubbles in viscous or turbulent shear stress ambient conditions. Furthermore, the unique action of the microbubbles caused by the Marangoni effect (Balasubramaniam et al., 1996; Leshansky et al., 2001) in heated space was found by Wang et al. (2007). In this context, the role of microbubbles in heat transfer does not diminish, in contrast to our expectations, but actually creates new thermal-hydraulic functions inside the thermal boundary layer.

In our previous work, natural convection heat transfer from a vertical heated plate in water with microbubble injection was investigated (Kitagawa and Murai, 2013). We found that the ratio of the heat transfer coefficient with bubble injection to that without bubble injection was 1.6−2.0 in both the laminar and transition regions (Fig. 1). In general, individual micro-bubbles have no potential to induce large liquid velocity fluctuations, since the Reynolds numbers of them are less than unity. In the experiments, rather than less individual action, we observed the intermittent wall-normal motion of a microbubble swarm during its rise, which was believed to enhance the time-averaged heat transfer.

With the ultimate goal of a comprehensive understanding of the role of microbubble swarm behavior in heat transfer enhancement, simplified experiments in the isothermal state are conducted to separate out the interference between the microbubbles' own buoyancy and the thermal buoyancy. One important point for problem setting in this paper is that the microbubble buoyancy can be intensified locally by the relative motion between the two phases, while the thermal buoyancy always obeys the diffusion process. The research into this topic is also motivated by the knowledge that microbubbles show regularized motion in terms of their slip velocity, while larger bubbles show turbulence-like complex motion to result in a diffusion process. A similar focus was reported by Watamura et al. (2013), who found preferential concentrations of microbubbles in Taylor-Couette flows, e.g., a negative diffusion coefficient for microbubbles in a shear flow. This microbubble physics may potentially be applied widely to mass, momentum, and heat transfer processes in chemical and mechanical engineering.

The outline of this paper is as follows. In Section 2, we explain the experimental setup, and in Section 3, we briefly describe the measurement technique. In Section 4, we discuss how the microbubble swarm behavior near a non-heated flat plate depends on the bubble diameter and the vertical bubble position, based on instantaneous and time-averaged bubble velocity data obtained using a particle tracking velocimetry (PTV) technique and visualization data at constant bubble flow rate. In Section 5, we give our conclusions.

2. Experimental setup

Fig. 2 shows a schematic diagram of the experimental apparatus. The apparatus consists of a transparent acrylic tank (1650 mm high, 310 mm wide and 150 mm deep), a flow straightener, a microbubble generator and a DC power supply (Takasago: ZX−400L). The flow straightener is used to reduce the liquid disturbances induced by the microbubble injection process. The microbubble generator is set at the bottom of the tank. The x, y, and z axes are set along the streamwise, wall-normal, and spanwise directions, respectively, and have zeros at the top of the microbubble generator, at the inner wall surface of the tank.

The hydrogen microbubbles are generated by water electrolysis (Hara et al., 2011). Salt is added to tap water at 22 ˚C to act as the electrolyte, with mass concentration of about 0.3 wt%. Using Faraday's law and the gas equation of state, the bubble volume flow rate Q is controlled by

$$Q = \frac{IR_0T_0}{2Fp}, \tag{1}$$

where I is the electric current through the electrodes, R_0 is the universal gas constant, T_0 is the water temperature, F is the Faraday constant, and p is the pressure.

Fig. 3 shows a schematic diagram of the microbubble generator. The generator mainly consists of two electrodes and a charcoal absorber. A platinum wire (0.1 or 0.2 mm diameter, 120 mm long) is used as the cathode, and a platinum pipe (3 mm outer diameter, 100 mm long) is used as the anode. The electric current through the electrodes is controlled by the DC power supply that was shown in Fig. 2. The width of the bubble exit from the generator is approximately 15 mm. The chlorine bubbles that are generated at the anode are completely eliminated by the charcoal absorber. In our experiments, bubbles are injected for 30 min before the start of experiment to increase the dissolved hydrogen concentration in the water. Therefore, the change in the bubble diameter that results from the dissolution of hydrogen inside the bubble is considered negligible. For reference, the relationship between the mean bubble diameter d_m and the bubble flow rate for different cathode diameters D, which was obtained by Kitagawa and Murai (2013), and accompanying bubble images are shown in Fig. 4. It is clear from Fig. 4 that d_m increases with increasing Q and decreasing D. The reason for this was explained by Kitagawa and Murai (2013).

3. Measurement technique

This study uses the PTV technique (Murai et al., 2006; Kitagawa et al., 2004) to measure the bubble velocity. Fig. 5 shows a schematic diagram of the bubble velocity measurement system. The measurement system consists of a monochrome charge coupled device (CCD) camera (IMPERX: VGA210−L), a diode-pumped solid state (DPSS) laser (Laser QUANTUM: excel mpc 6000), cylindrical lenses, a neutral density (ND) filter and a PC. The DPSS laser is set at the side of the tank, and the 2-mm-thick laser light sheet (which is produced using the two cylindrical lenses) illuminates the bubbles. As a result, the image captures the laser light that is scattered at the bubble interface. The frame rate and the shutter speed are 200 fps and 1/1,000 s, respectively. The PC records 640×480-pixel images taken with the CCD camera. Table 1 lists the experimental conditions used for the bubble velocity measurements. The bubble velocity measurements are taken in the x-y plane. The measurement area for the bubble velocity measurements is 20.1×15.1 mm^2.

The procedure used to estimate the bubble velocity is as follows. The bubble centroid is estimated by application of the particle mask correlation method (Takehara and Etoh, 1999) to images that capture the laser light scattered at each bubble. In our experiments, the bubble diameter is much smaller than the laser light sheet thickness, and thus the laser light scattered at each bubble interface can be treated in the same way as the liquid tracer particles that are commonly used in the PTV technique. The bubble velocity vector is estimated using the three-step-tracking method (e.g., Kitagawa et al., 2004). To obtain reliable statistical data, 6,000 images are used for each set of experimental conditions. The uncertainty in the bubble velocity associated with the detection of the bubble centroid is estimated to be 1.9 mm/s. In addition, the error in this value is estimated to be 3.3 % of the maximum value of the bubble rise velocity (58.2 mm/s).

4. Results and discussion

In Section 4, we discuss the dependence of both the bubble diameter and the vertical bubble position on the microbubble swarm behavior. For Q=42 mm^3/s, the mean bubble diameter is 71 μm for D=0.1 mm and 41 μm for D=0.2 mm (Fig. 4). Under the experimental conditions given, the Weber number and the bubble Reynolds number based on the terminal velocity are less than 0.1 and 1, respectively. Thus, all the bubbles are almost spherical, and no unsteady wakes are produced behind the individual bubbles.

4.1. Probability density distribution of bubbles

Fig. 6 shows the probability density distributions of the microbubbles, Γ. At x=500 mm, the distribution has its highest peak near the wall contact limit for both diameters. A similar phenomenon is also seen in an upward co-current bubbly two-phase flow in a channel or pipe. For example, Takagi and Matsumoto (2011) found that bubbles in a vertical turbulent channel flow accumulated close to the wall because of the lift force (Auton, 1987), and that the bubble clusters formed along the wall modified the boundary layer turbulence structures. In contrast, in the present study, no base flow is given to the liquid phase in this container. Thus, the microbubbles drive the upward liquid flow around the wall, and this flow pushes the microbubbles toward the wall because of the lift force in the range of the positive liquid velocity gradient. Further analysis of the results shows that the distribution near the wall has a lower value for d_m=41 μm than that for d_m=71 μm. This indicates that small bubbles promote greater diffusion in the wall-normal direction than the larger bubbles. This trend reflects the peak in the distribution that continuously decreases in the x direction, particularly between x=250 and 500 mm.

4.2. Bubble rise velocity

In this section, we first discuss the relationship between the microbubble-liquid relative velocity u_s (i.e., the terminal velocity of a single microbubble) and the ambient liquid rise velocity u_L against the rise velocity of the microbubbles. The terminal velocity of a single bubble, u_{TW}, in a stationary liquid is obtained from the force balance equation between the drag, F_D, and the buoyancy, F_B, acting on the bubble. F_D and F_B are given by

$$F_D = 4\pi\mu_L u_{TW}\left(\frac{d_m}{2}\right)\left(1+\frac{3}{8}\cdot\frac{d_m}{2y}\right), \tag{2}$$

$$F_B = (\rho_L - \rho_G)\frac{4}{3}\pi\left(\frac{d_m}{2}\right)^3 g, \tag{3}$$

where μ_L is the viscosity of water, y is the distance from the wall to the bubble centroid, ρ_L is the density of water, ρ_G is the density of hydrogen and g is the gravitational acceleration. Eq. (2) represents the Stokes drag force when taking the wall effect into account, which was theoretically obtained by Takemura et al. (2002). Based on Eqs. (2) and (3), the terminal velocity of a single bubble rising near the wall is given by

$$u_{TW} = \frac{(\rho_L - \rho_G)g d_m^2}{12\mu_L\left(1+3d_m/16y\right)}, \quad 2y > d_m. \tag{4}$$

Fig. 7 shows the profiles of $(u-u_{TW})/u$, where u is the mean rise velocity of the microbubbles. This figure shows only the results in the region where the bubbles exist, based on the results shown in Fig. 6. For both values of d_m, $(u-u_{TW})/u$ is approximately 0.9. This result indicates that u is much higher than u_{TW}, and that u is approximately equal to u_L, considering that $u=u_S+u_L=u_{TW}+u_L$. Therefore, the microbubbles cause the high-speed upward liquid flow. As described earlier, in our experiments, the bubble Reynolds number is less than unity for

both values of d_m. Therefore, in terms of the bubble-liquid relative coordinates, the flow around an individual bubble can be regarded as a Stokes flow. In the Stokes flow, the momentum diffusion length is sufficiently long, meaning that the bubble-induced liquid entrainments interact strongly with each other over a wide range. For this reason, the high-speed upward liquid flow is induced, not by the buoyancy of each bubble, but by the spatial buoyancy distribution of bubbles. These are important properties of the two-phase flows that are induced by multiple microbubbles near the wall.

Fig. 8 shows the mean rise velocity profiles of the microbubbles. At x=500 mm, in the y=0−3.3 mm range, u is higher for d_m=71 μm than for d_m=41 μm. Moreover, in the y=0−3.3 mm range, u for d_m=41 μm decreases with increasing x. As expected, these results are closely related to the buoyancy distribution of the bubbles. An interesting illustration of the relationship between Γ and u is given in Fig. 9, which is obtained based on a comparison of Figs. 6 and 8. For reference, the relationship between the profiles of the temperature T and the liquid velocity u_L for laminar natural convection without bubbles that was obtained from our numerical simulations is shown in Fig. 10. Details of these numerical simulations are given in Appendix A. For both values of d_m, the profile of Γ has a peak at the wall, while that of u has a peak some distance away from the wall (Fig. 9). The former is due to the lift force that is acting on the bubble, and the latter is due to the viscous resistance. Similar relationships between the buoyancy and velocity profiles are also seen in Fig. 10. This similarity results in active interactions between the microbubbles and the natural convection process, and is therefore the primary reason for the enhancement of natural convection heat transfer by microbubble injection (Kitagawa and Murai, 2013). This relationship between the buoyancy and the velocity profiles appears only when the bubble diameter is quite small, and becomes indistinct in flows with millimeter- or sub-millimeter-scale bubbles (Kitagawa et al., 2009) (Fig. 11).

4.3 Bubble velocity versus bubble-bubble distance

Fig. 12 shows the temporal changes in the rise velocity averaged over all bubbles in a search region u_a and the mean bubble-bubble distance L_a, which is defined as

$$L_a = \frac{\sum_{i=1}^{N} \sqrt{(x_i - x_{near})^2 + (y_i - y_{near})^2}}{N}, \tag{5}$$

where x_i and y_i are the centroids of a focused bubble in the search region, x_{near} and y_{near} are the centroids of the bubble nearest to the focused bubble and N is the total number of bubbles in the search region. The search region is set at 495<x<505 mm and 0<y<4 mm. For reference, the root mean square (RMS) value of u_a' (i.e. the fluctuation of u_a), $\langle u_a' u_a' \rangle^{1/2}$, is shown in this figure. Figs. 13 and 14 show the frequency spectra of u_a and the cross-correlation between L_a' (i.e. the fluctuation of L_a) and u_a', respectively. The cross-correlation is defined as

$$R_u(\tau) = \frac{\overline{L_a'(t) u_a'(t+\tau)}}{\sqrt{\overline{L_a'^2}}\sqrt{\overline{u_a'^2}}}, \tag{6}$$

where τ is the time delay. At x=500 mm, $\langle u_a' u_a' \rangle^{1/2}$ is higher for d_m=41 μm than for d_m=71 μm (Fig. 12(a) and (c)). In the low frequency range (i.e. less than 1 Hz), the u_a spectrum is higher for d_m=41 μm than for d_m=71 μm (Fig. 13). This is because, near the wall, the pulsatory rise of the microbubble swarm occurs markedly for small bubbles. In particular, in the case where d_m=41 μm, u_a tends to increase at smaller values of L_a (Fig. 12(c)). This is caused by an increase in the local buoyancy source that results from an accumulation of bubbles, and suggests that there is a negative correlation between u_a' and L_a'. This negative correlation is also clearly shown in Fig. 14. This trend indicates that the pulsatory rise of the microbubble swarm is strongly dependent on the generation of

bubble number density waves within the swarm. However, for d_m=71 μm, there is no such tendency between u_a and L_a (Fig. 12(a)). In addition, the negative cross-correlation between u_a' and L_a' for d_m=41 μm can be seen more clearly at x=500 mm when compared with that at x=250 mm (Fig. 12(b) and (c), and Fig. 14), and the u_a spectrum in the low frequency range is higher at x=500 mm than at x=250 mm (Fig. 13). These trends imply that the amplification of the bubble number density waves within the microbubble swarm causes a significant pulsatory rise of the swarm in the downstream region.

Fig. 15 shows the temporal changes in the wall-normal velocity averaged over the bubbles in a search region, v_a, and L_a. The search region used here is the same as that used in Fig. 12 (i.e., 495<x<505 mm and 0<y<4 mm). For reference, the RMS value of v_a' (i.e. the fluctuation of v_a), $\langle v_a' v_a' \rangle^{1/2}$, is shown in this figure. Fig. 16 shows the cross-correlation between L_a' and v_a', which is defined as

$$R_v(\tau) = \frac{\overline{L_a'(t) v_a'(t+\tau)}}{\sqrt{\overline{L_a'^2}}\sqrt{\overline{v_a'^2}}}. \tag{7}$$

At x=500 mm, $\langle v_a' v_a' \rangle^{1/2}$ is higher for d_m=41 μm than for d_m=71 μm (Fig. 15(a) and (c)). This is the same tendency as that shown in Fig. 12(a) and (c). For d_m=41 μm, v_a is positive at smaller values of L_a and becomes negative at larger L_a (Fig. 15(c)). This indicates that there is a negative cross-correlation between v_a' and L_a'. This negative cross-correlation can also be seen in Fig. 16. This trend suggests that the bubbles move away from the wall when bubble accumulation occurs, while the bubbles move toward the wall when the bubble number density is low. For d_m=41 μm, the fluctuations of both v_a and L_a are larger at x=500 mm than at x=250 mm (Fig. 15(b) and (c)), and the negative cross-correlation between v_a' and L_a' can be seen more clearly at x=500 mm than at x=250 mm (Fig. 16).

4.4 Wall-normal behavior of the bubble swarm

In this section, we discuss in detail the wall-normal behavior of microbubble swarms. Fig. 17 shows typical time series of images of the bubbles near the wall for d_m=41 μm at x=500 mm. In the upstream region, the bubbles rise along the wall under an almost regular configuration because of the lift-locking effect of the mean liquid velocity gradient. As the bubbles rise, bubble clouds are then formed in the swarm, probably by bubble-bubble interactions (Kitagawa et al., 2004), which are shown in Fig. 17(a). Because of their different rise velocities, these bubble clouds collide and coalesce (Fig. 17(c)), and as a result, a large-scale bubble cloud detaches from the wall (Fig. 17(e)). Note that since the size of bubble clouds is roughly the same as the mean bubble layer thickness near the wall, bubble clouds are non-uniformly distributed in only the stream-wise and span-wise directions.

The typical bubble fluctuation velocity vector distributions at x=500 mm are shown in Fig. 18 to help us understand the behavior of bubble clouds close to the wall. The fluctuation velocity vector color is red when the wall-normal velocity is positive and blue when the velocity is negative. Because of differences in the local buoyancy sources, there is a difference in the rise velocities between the front bubble cloud A and the rear bubble cloud B. This velocity difference leads to the interaction between the two bubble clouds. Because of this interaction, cloud A moves toward the wall, while cloud B starts to move away from the wall (Fig. 18(a)). Cloud A is then directly affected by the wall, and as a result, has a downward fluctuation velocity. In contrast, cloud B moves rapidly away from the wall because of the blocking effect of the low-speed cloud A. Then, this interaction between the clouds involves bubbles that are far from the wall, and forces them to move toward the wall (Fig. 18(c)). Moreover, based on the distributions of u_a' and v_a' for about 2.5 s obtained from Figs. 12 and 15, the distribution for d_m=41 μm becomes non-isotropic, and the positive correlation between u_a' and v_a' is induced by

the cloud interaction (Fig. 19(a)). In contrast, no similar trend occurs for d_m=71 μm (Fig. 19(b)). The series of motions for d_m=41 μm is like a bursting motion (Robinson, 1991; Lumley and Blossey, 1998) that occurs in turbulent flows (Fig. 18(b)). Thus, we term this motion the "void-bursting motion", and consider it to be one of the unique motion characteristics of the microbubble swarm rising near the wall. It is concluded from these results that the temporal change in the sign of v_a for d_m=41 μm (which was shown in Fig. 15) is a result of this void-bursting motion.

Fig. 20 shows the relationship between the large bubble cloud formation frequency and δ_{Bav}/δ_{av}, where δ_{Bav} is the mean bubble layer thickness when a large bubble cloud is formed (i.e., when the interaction of the bubble clouds occurs) and δ_{av} is the time-averaged bubble layer thickness δ. The frequency is significant for d_m=41 μm (i.e., high bubble number density). In addition, the frequency is higher at x=250 mm than at x=500 mm, but the opposite applies for δ_{Bav}/δ_{av}. According to our bubble image analysis, the void-bursting motion barely occurs at x=250 mm. For these reasons, the generation of the void-bursting motion requires not only the interaction of the bubble clouds but also the growth of bubble clouds caused by the interaction while the bubbles rise.

From the results above, the void-bursting motion generation mechanism and the effects of this motion on Γ and u can be summarized as follows (Fig. 21). At a constant bubble flow rate, the local bubble number density is higher for d_m=41 μm than for d_m=71 μm just after the microbubble injection. For d_m=41 μm, the bubble-bubble interactions probably occur because of the fairly high initial bubble number density. The bubble-bubble interactions collapse the initial bubble configuration, and, as a result, small-scale bubble clouds are formed locally. Then, near the wall, the void-bursting motion arises from the interaction of the bubble clouds that had grown. It should be noted that no such phenomenon has been reported for non-microbubble flows. In contrast, for d_m=71 μm, the terminal rise velocity is relatively high, and the initial bubble number density is low. Thus, the bubble-bubble interactions are inactive, and the bubble clouds that cause the void-bursting motion barely occur. When the void-bursting motion does arise, the bubble diffusion in the wall-normal direction is enhanced, and the local bubble number density (i.e., the local buoyancy source) near the wall decreases with increases in x. This causes a reduction in the upward liquid flow, so that the bubble rise velocity also decreases. Because of this process, Γ and u are lower for d_m=71 μm than for d_m=41μm (Figs. 6 and 8). In addition, far away from the wall, increases in Γ and u depend strongly on the generation of the void-bursting motion (Fig. 8).

5. Conclusions

To answer the question why natural convection heat transfer from a vertical heated flat plate is dramatically enhanced by microbubble injection, microbubble swarm behavior in an isothermal ambient was investigated experimentally. Two different microbubble sizes that do not produce individual wakes were examined at a constant bubble volume flow rate. Space- and time-resolved measurements of the microbubble behavior inside the swarm by PTV have led us to the following conclusions.

Microbubbles drive the liquid upward flow around the wall, and this flow reaches its highest velocity at a distance outside the microbubble mixture layer. This leads to the lift force that pushes the microbubbles toward the wall (i.e. the lift-locking effect). Because of this lift force, the probability density distribution of the microbubbles has its highest peak near the wall contact limit. As a result, the near-wall buoyancy intensifies, and this causes the liquid upward flow to speed up. Moreover, both the velocity and buoyancy profiles for the microbubble mixture are analogous to the same profiles for single-phase natural convection from a heated wall. This results in active interactions between the microbubbles and natural convection, and is one of the reasons why natural convection heat transfer is magnified by the injection of microbubbles.

The microbubble swarm shows a significant pulsatory rise along the wall, particularly for small bubbles. This

behavior is strongly dependent on the generation of bubble number density waves within the swarm, and amplification of the waves in the downstream region results in void-bursting motion (i.e. the large-scale separation of the grown bubble clouds from the wall) in the final stage. The void-bursting motion is characterized by the negative correlation between the bubble-bubble distance and the wall-normal velocity of the bubbles. That means that only the clouds that contain dense microbubbles are ejected from the wall, overshadowing the lift-locking effect of the mean liquid velocity gradient. The void-bursting motion can transport a large volume of liquid from the near-wall layer to the outside, and this activates heat transfer process dramatically. The phenomena observed in this study look like the excitation of a transition to turbulent heat transfer from one viewpoint, but the underlying mechanism of the void-bursting motion is completely different from that process and cannot be approximated with a single-phase description because the microbubble mixture behaves like a buoyant fluid with a negative diffusion coefficient (i.e. the lift-locking effect). These unique characteristics of microbubbles not only induce the pulsatory rise of the microbubble swarm but might also produce further intrinsic phenomena associated with the diffusion processes for mass, momentum, and energy.

Nomenclature

D	cathode diameter, mm
d_m	mean bubble diameter, μm
F	Faraday constant, C/mol
F_D	drag acting on bubble, N
F_B	buoyancy acting on bubble, N
g	gravitational acceleration, m/s^2
I	electric current through electrode, A
L_a	mean bubble-bubble distance in search region, mm
N	total number of bubbles in search region
p	pressure, Pa
Q	bubble volume flow rate, mm^3/s
R_0	universal gas constant, J/(K mol)
T_0	water temperature, K
u	mean bubble rise velocity, mm/s
u_a	rise velocity averaged over bubbles in search region, mm/s
u_a'	fluctuation of u_a, mm/s
u_{TW}	terminal velocity of single bubble rising near wall, mm/s
v_a	wall-normal velocity averaged over bubbles in search region, mm/s
v_a'	fluctuation of v_a, mm/s
x, y, z	streamwise, wall-normal, and spanwise directions
x_i, y_i	centroids of focused bubble in search region
x_{near}, y_{near}	centroids of nearest bubble to focused bubble

Greek symbols

δ	bubble layer thickness, mm
δ_{av}	time average of δ, mm
δ_{Bav}	mean bubble layer thickness when large bubble cloud is formed, mm

μ_L viscosity of water, Pa s
ρ_G density of hydrogen, kg/m^3
ρ_L density of water, kg/m^3

Acknowledgments

The authors gratefully acknowledge the support of a Grant-in-Aid for Scientific Research (A) (grant no. 24246033). In addition, the authors wish to thank Mr. T. Ozato of Kyoto Institute of Technology for his assistance with data collection.

Appendix A. Supporting information

Appendix A can be found in the supporting information.

References

Auton, T.R., 1987. The lift force on a spherical body in a rotational flow. Journal of Fluid Mechanics 183, 199-218.

Balasubramaniam, R., Lacy, G., Wozniak, G., Subramanian, R.S., 1996. Thermocapillary migration of bubbles and drops at moderate Marangoni number in reduced gravity. Physics of Fluids 8, 872-880.

Celata, G.P., Chiaradia, A., Cumo, M., D'Annibale, F., 1999. Heat transfer enhancement by air injection in upward heated mixed-convection flow of water. International Journal of Multiphase Flow 25, 1033-1052.

Dhir, V., 1998. Boiling heat transfer. Annual Review of Fluid Mechanics 30, 365-401.

Dressaire, E., Bee, R., Bell, D.C., Lips, A., Stone, H.A., 2008. Interfacial polygonal nanopatterning of stable microbubbles. Science 320, 1198-1201.

Hara, K., Suzuki, T., Yamamoto, F., 2011. Image analysis applied to study on frictional-drag reduction by electrolytic microbubbles in a turbulent channel flow. Experiments in Fluids 50, 715-727.

Ivashnyov, O.E., Smirnov, N.N., 2004. Thermal growth of a vapor bubble moving in superheated liquid. Physics of Fluids 16, 809-823.

Johnson, B.D., Cooke, R.C., 1981. Generation of stabilized microbubbles in seawater. Science 213, 209-211.

Kenning, D.B.R., Kao, Y.S., 1972. Convective heat transfer to water containing bubbles: Enhancement not dependent on thermocapillarity. International Journal of Heat and Mass Transfer 15, 1709-1717.

Kitagawa, A., Murai, Y., 2013. Natural convection heat transfer from a vertical heated plate in water with microbubble injection. Chemical Engineering Science 99, 215-224.

Kitagawa, A., Sugiyama, K., Murai, Y., 2004. Experimental detection of bubble-bubble interactions in a wall-sliding bubble swarm. International Journal of Multiphase Flow 30, 1213-1234.

Kitagawa, A., Uchida, K., Hagiwara, Y., 2009. Effects of bubble size on heat transfer enhancement by sub-millimeter bubbles for laminar natural convection along a vertical plate. International Journal of Heat and Fluid Flow 30, 778-788.

Legendre, D., Boree, J., Magnaudet, J., 1998. Thermal and dynamic evolution of a spherical bubble moving steadily in a superheated or subcooled liquid. Physics of Fluids 10, 1256-1272.

Leshansky, A.M., Lavrenteva, O.M., Nir, A., 2001. Thermocapillary migration of bubbles: convective effects at low Peclet number. Journal of Fluid Mechanics 443, 377-401.

Llewellina, E.W., Manga, M., 2005. Bubble suspension rheology and implications for conduit flow. Journal of

Volcanology and Geothermal Research 143, 205-217.
Lumley, J., Blossey, P., 1998. Control of turbulence. Annual Review of Fluid Mechanics 30, 311-327.
Makuta, T., Takemura, F., Hihara, E., Matsumoto, Y., Shoji, M., 2006. Generation of micro gas bubbles of uniform diameter in an ultrasonic field. Journal of Fluid Mechanics 548, 113-131.
Murai, Y., Oishi, Y., Takeda, Y., Yamamoto, F., 2006. Turbulent shear stress profiles in a bubbly channel flow assessed by particle tracking velocimetry. Experiments in Fluids 41, 343-352.
Robinson, S.K., 1991. Coherent motions in the turbulent boundary layer. Annual Review of Fluid Mechanics 23, 601-639.
Suslov, S.A., Ooi, A., Manasseh, R., 2012. Nonlinear dynamic behavior of microscopic bubbles near a rigid wall. Physical Review E 85, 66309
Takagi, S., Matsumoto, Y., 2011. Surfactant effects on bubble motion and bubbly flows. Annual Review of Fluid Mechanics 43, 615-636.
Takehara, K., Etoh, T., 1999. A study on particle identification in PTV, Journal of Visualization 1, 313-323.
Takemura, F., Takagi, S., Magnaudet, J., Matsumoto, Y., 2002. Drag and lift force on a bubble rising near a vertical wall in a viscous Liquid. Journal of Fluid Mechanics 461, 277-300.
Timkin, L.S., Gorelik, R.S., 2009. The problems of the upward monodispersed microbubble flow in a vertical tube. Journal of Engineering Thermophysics 18, 69-71.
Tokuhiro, A.T., Lykoudis, P.S., 1994. Natural convection heat transfer from a vertical plate-I. Enhancement with gas injection. International Journal of Heat and Mass Transfer 37, 997-1003.
Wang, H., Peng, X., Garimell, S.V., Christopher, D.M., 2007. Microbubble return phenomena during subcooled boiling on small wires, International Journal of Heat and Mass Transfer 50, 163-172.
Watamura, T., Tasaka, Y., Murai, Y., 2013. Intensified and attenuated waves in a microbubble Taylor-Couette flow. Physics of Fluids 25, 054107
Yang, B., Prosperetti, A., 2008. Vapour bubble collapse in isothermal and non-isothermal liquids. Journal of Fluid Mechanics 601, 253-279.

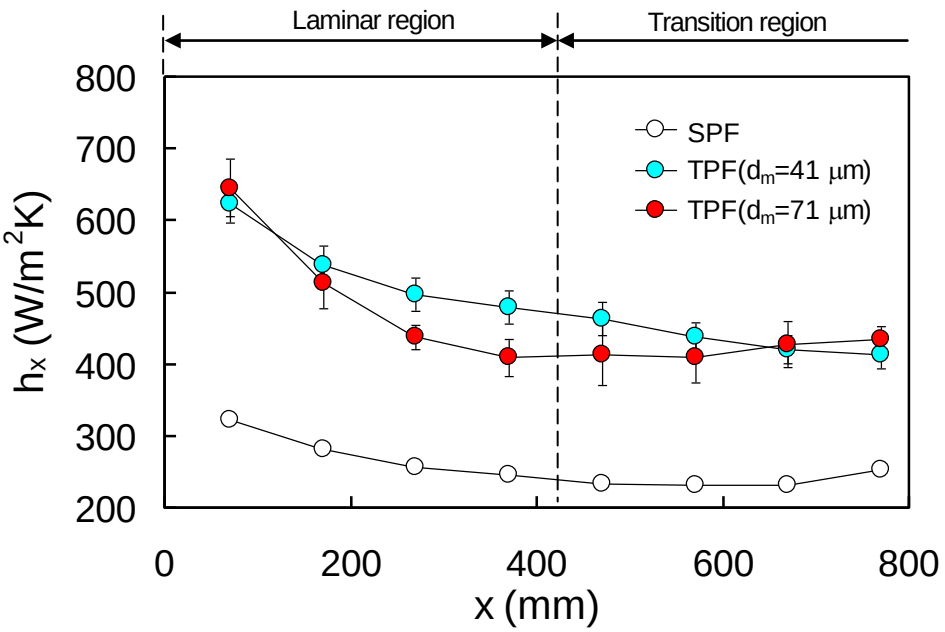

Fig. 1. Relationship between measurement location x and heat transfer coefficient h_x. SPF stands for single-phase flow, TPF stands for two-phase flow, and d_m is mean bubble diameter. From Kitagawa and Murai (2013).

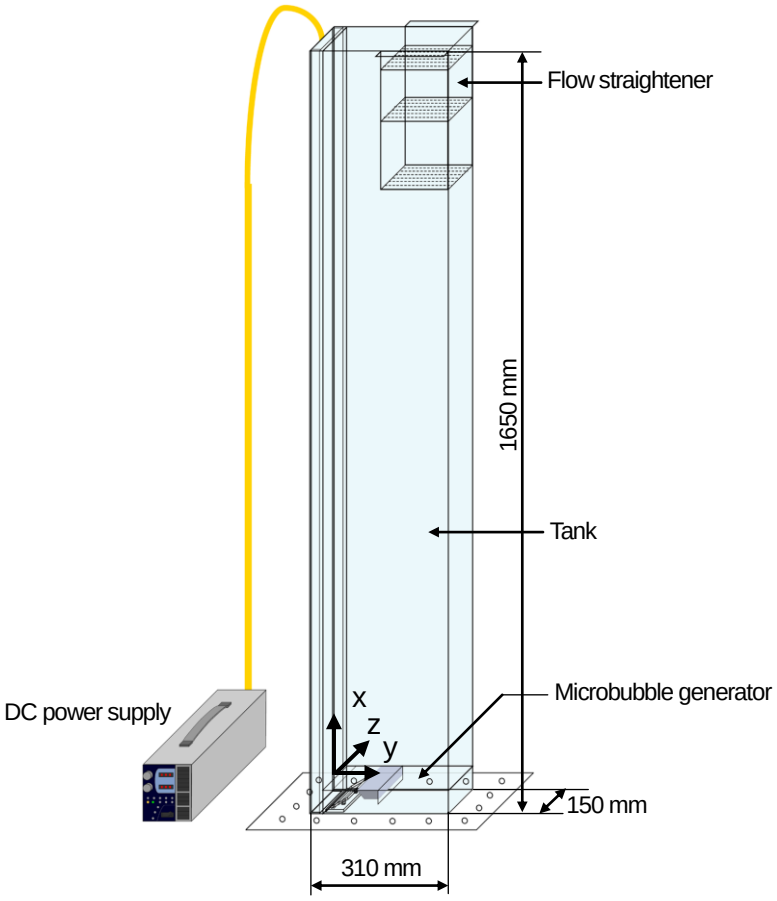

Fig. 2. Schematic diagram of the experimental apparatus.

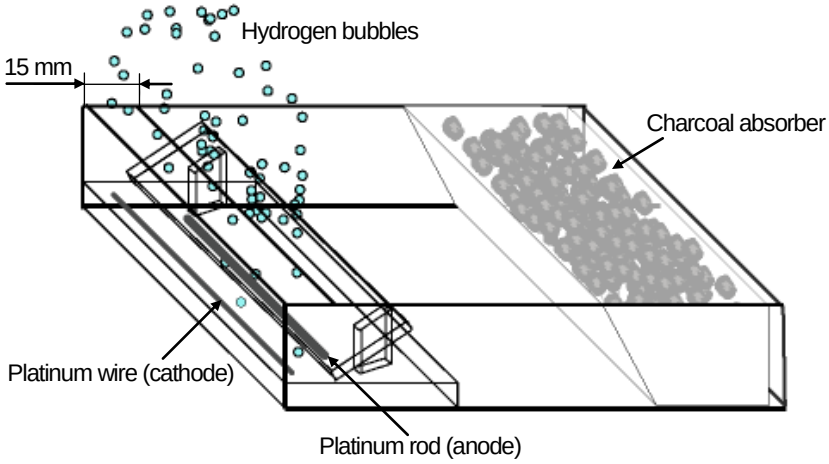

Fig. 3. Schematic diagram of the microbubble generator.

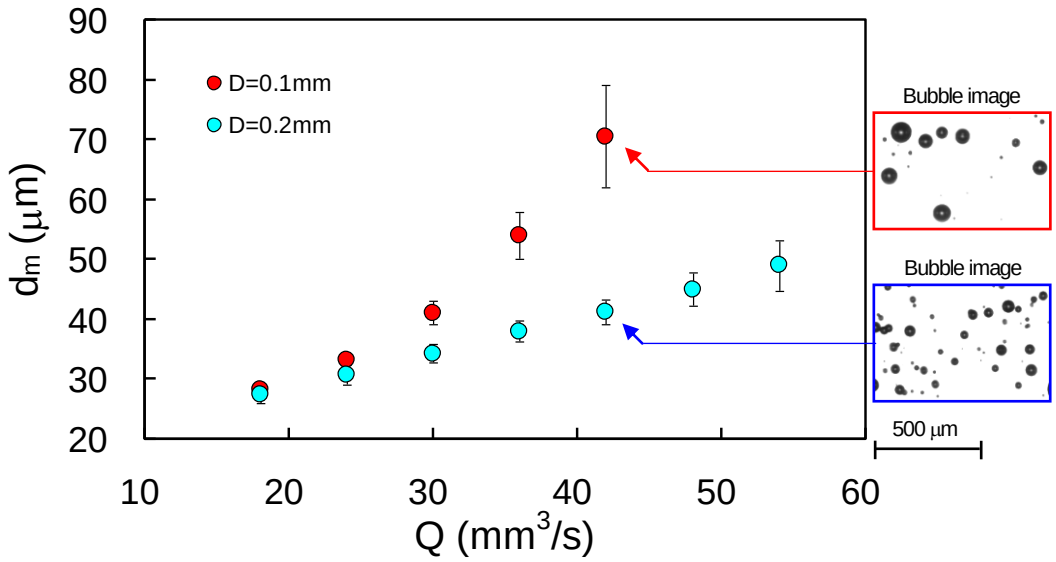

Fig. 4. Relationship between Q and d_m for different cathode diameters. From Kitagawa and Murai (2013).

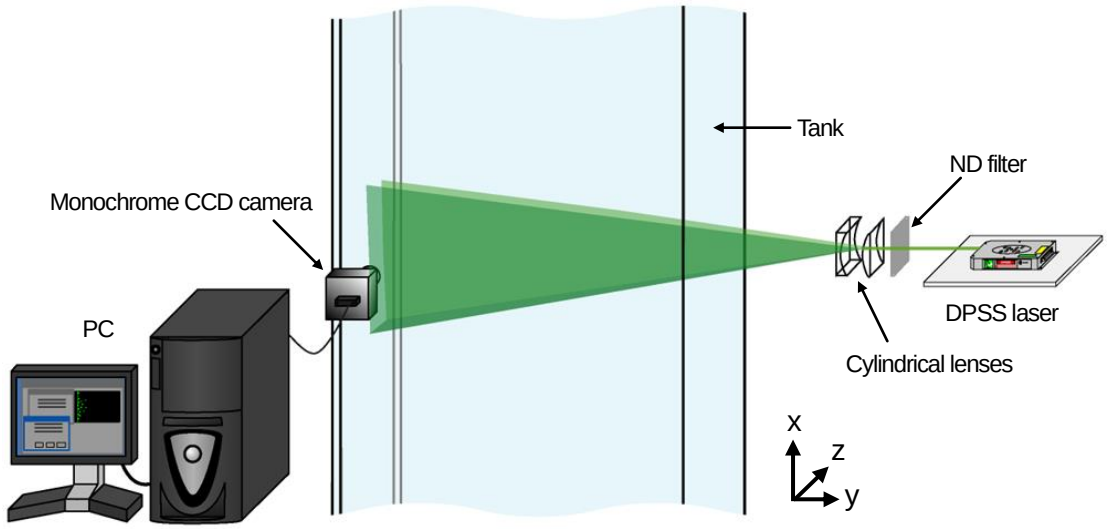

Fig. 5. Schematic diagram of the bubble velocity measurement system.

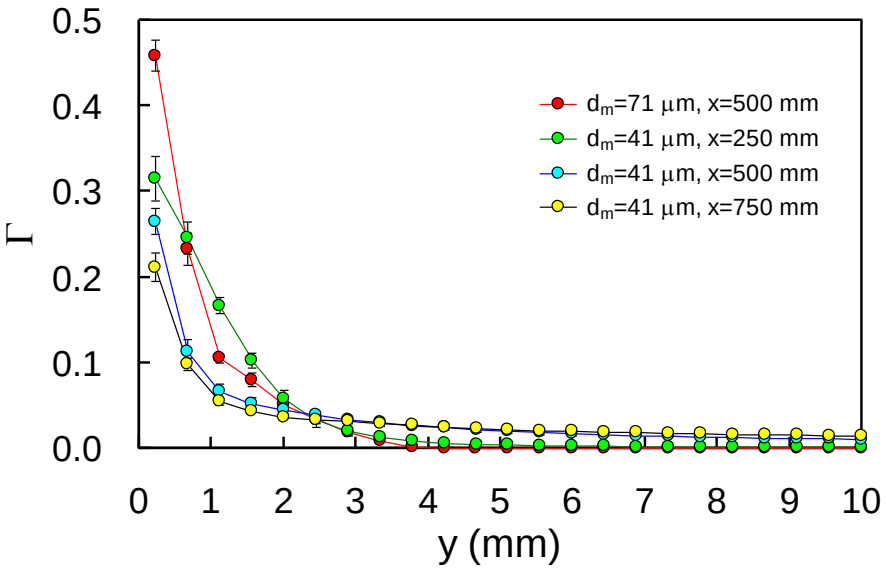

Fig. 6. Probability density distributions of microbubbles.

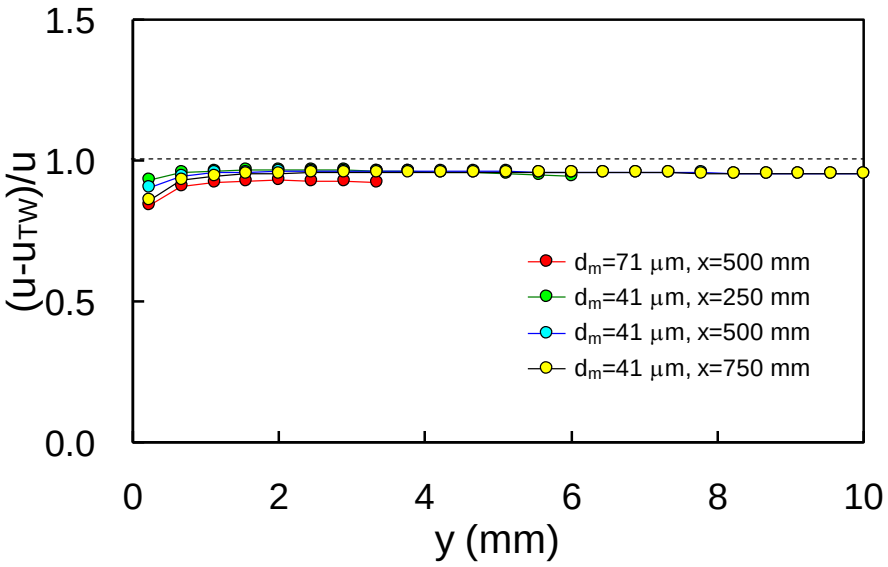

Fig. 7. Profiles of $(u–u_{TW})/u$.

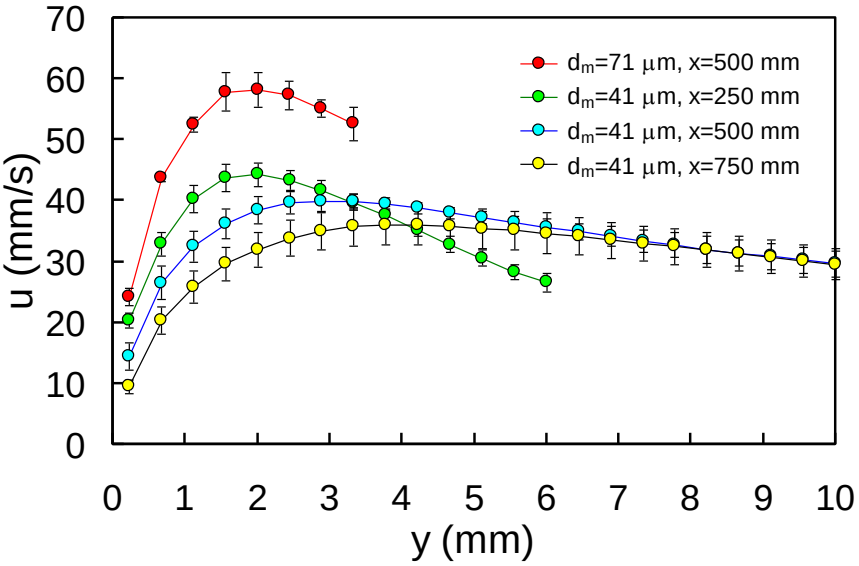

Fig. 8. Profiles of mean rise velocity of microbubbles.

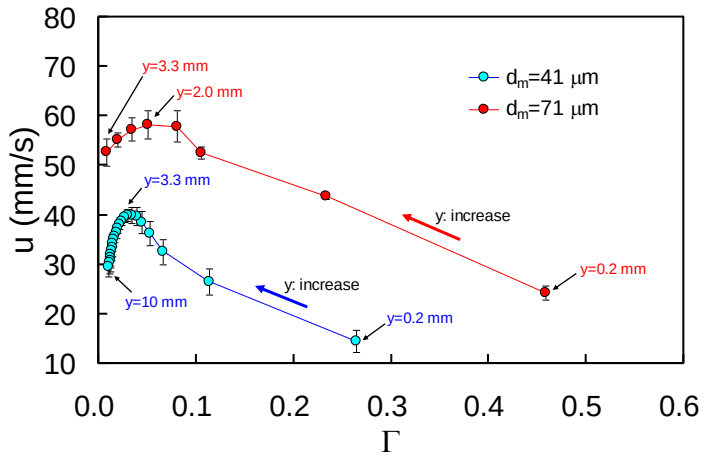

Fig. 9. Relationship between Γ and u at x=500 mm.

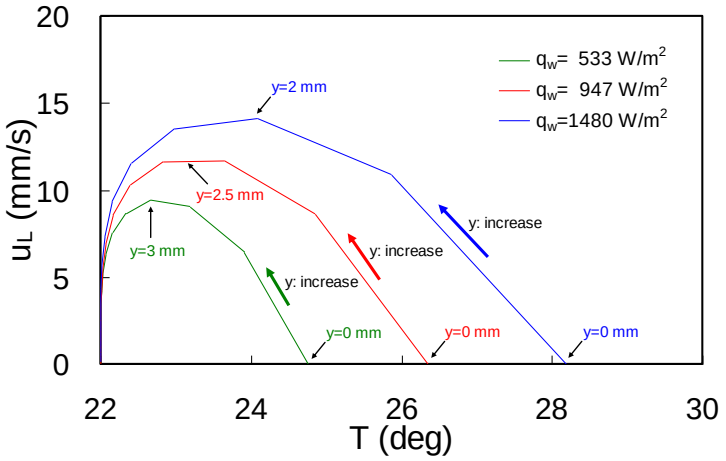

Fig. 10. Relationship between T and u_L in laminar region (simulation results).

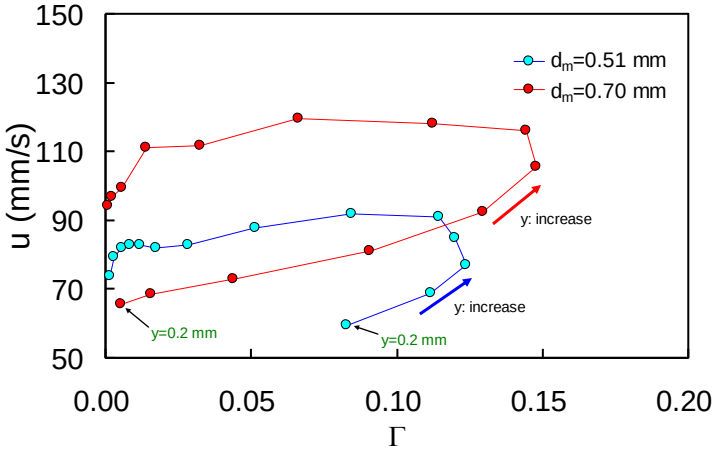

Fig. 11. Relationship between Γ and u at x=170 mm for sub-millimeter-bubble flows obtained using Kitagawa et al.'s experimental results (Kitagawa et al., 2009).

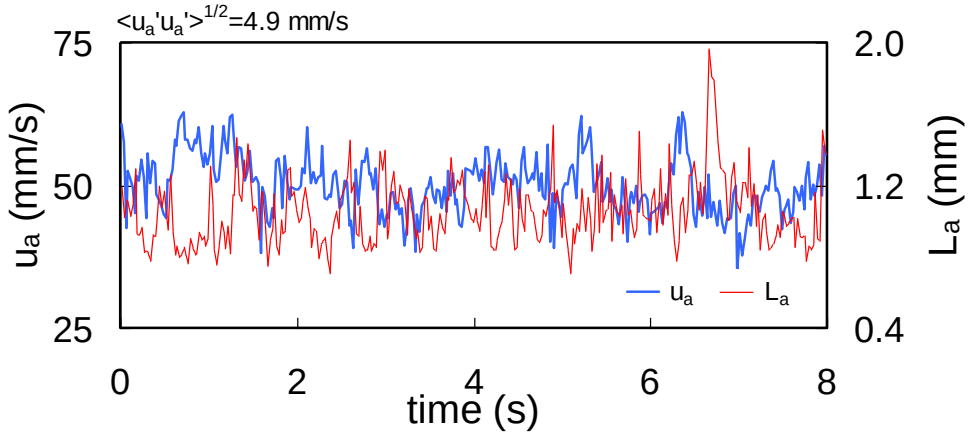

(a) d_m=71 μm and x=500 mm

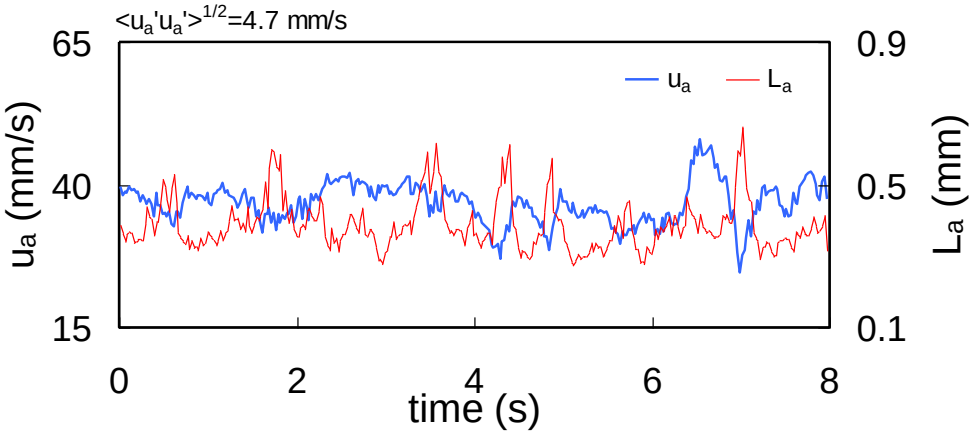

(b) d_m=41 μm and x=250 mm

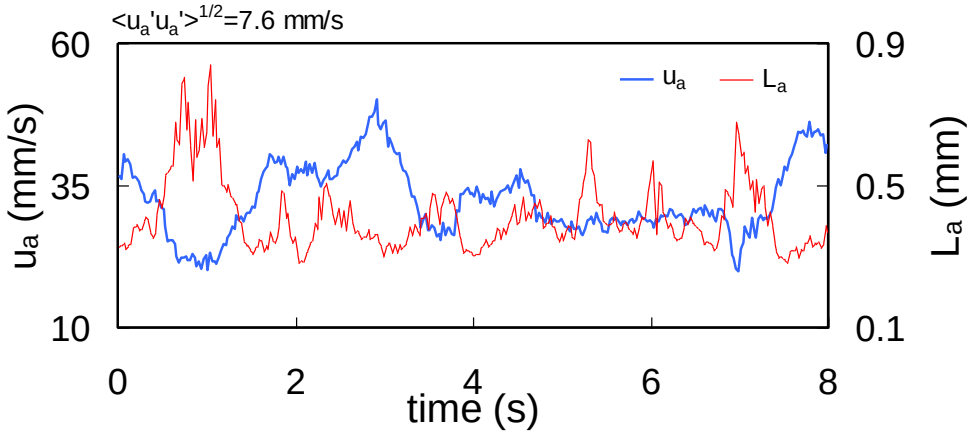

(c) d_m=41 μm and x=500 mm

Fig. 12. Temporal changes in u_a and L_a.

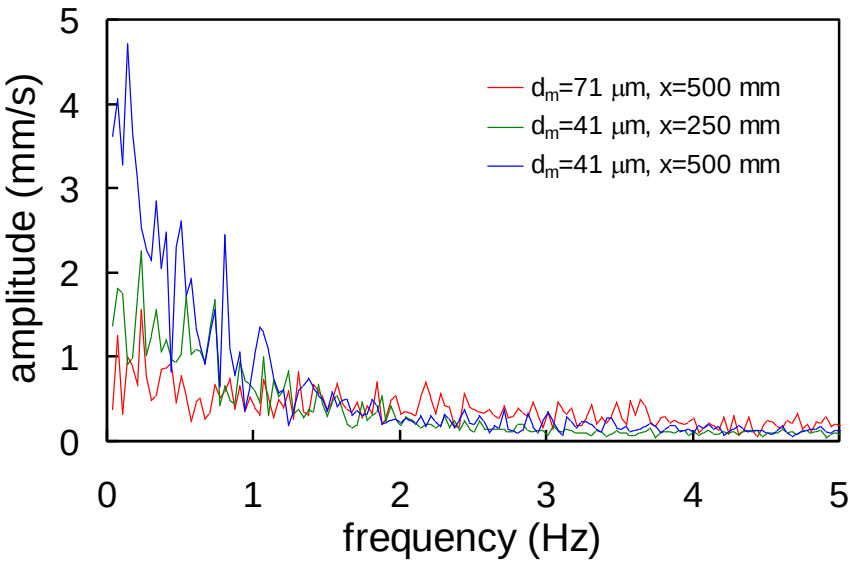

Fig. 13. Spectrum of u_a.

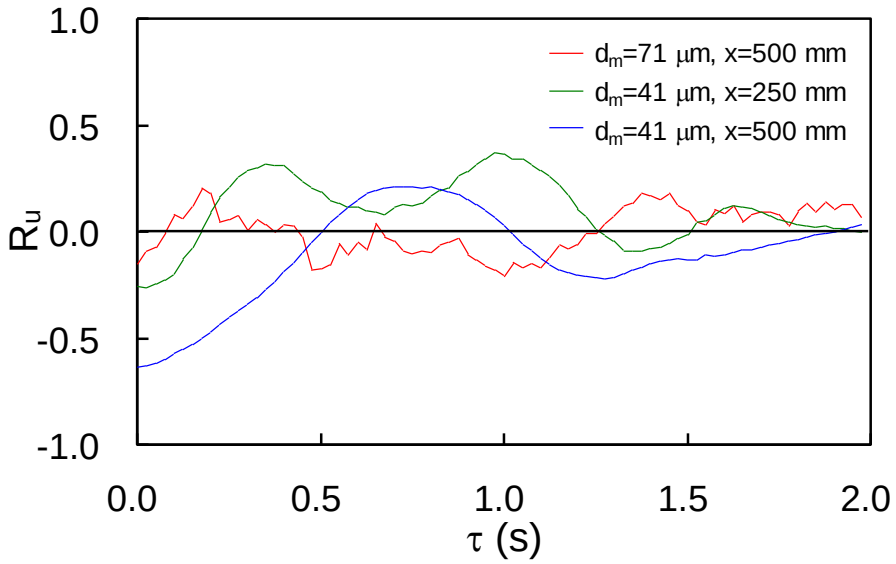

Fig. 14. Cross-correlation between L_a' and u_a'.

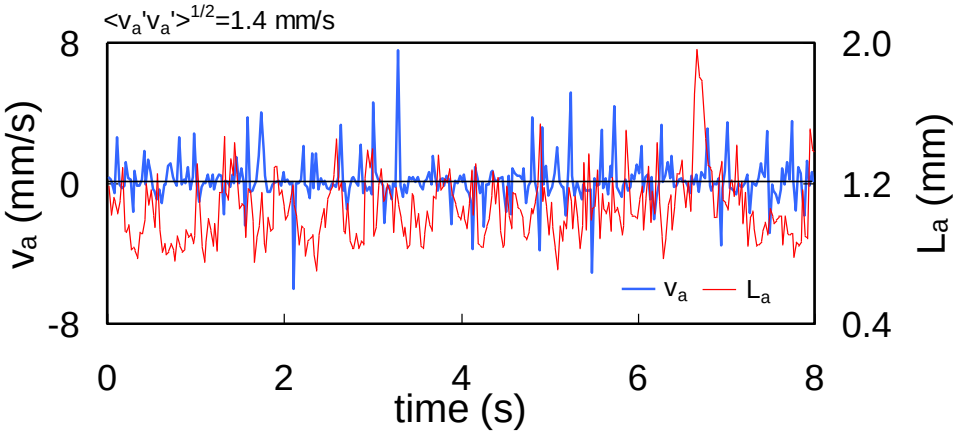

(a) d_m=71 μm and x=500 mm

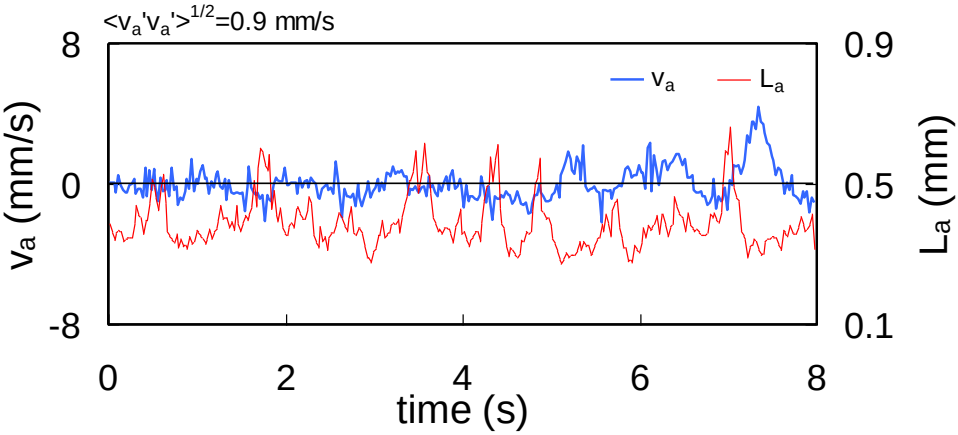

(b) d_m=41 μm and x=250 mm

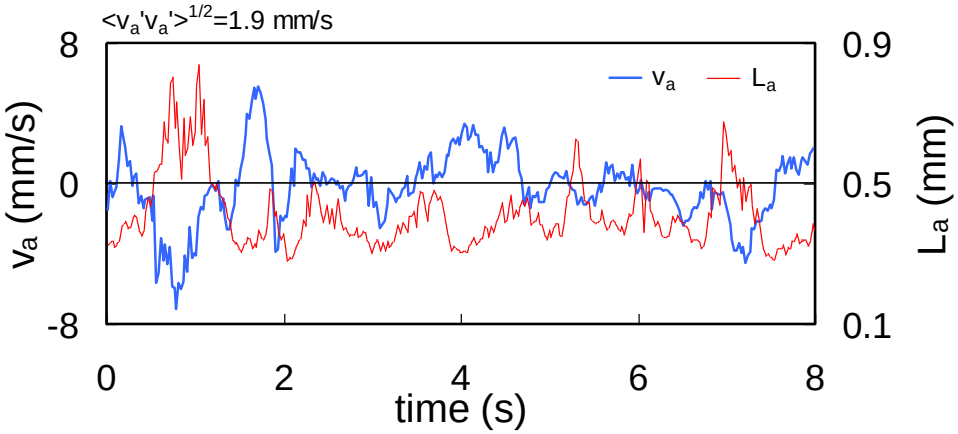

(c) d_m=41 μm and x=500 mm

Fig. 15. Temporal changes in v_a and L_a.

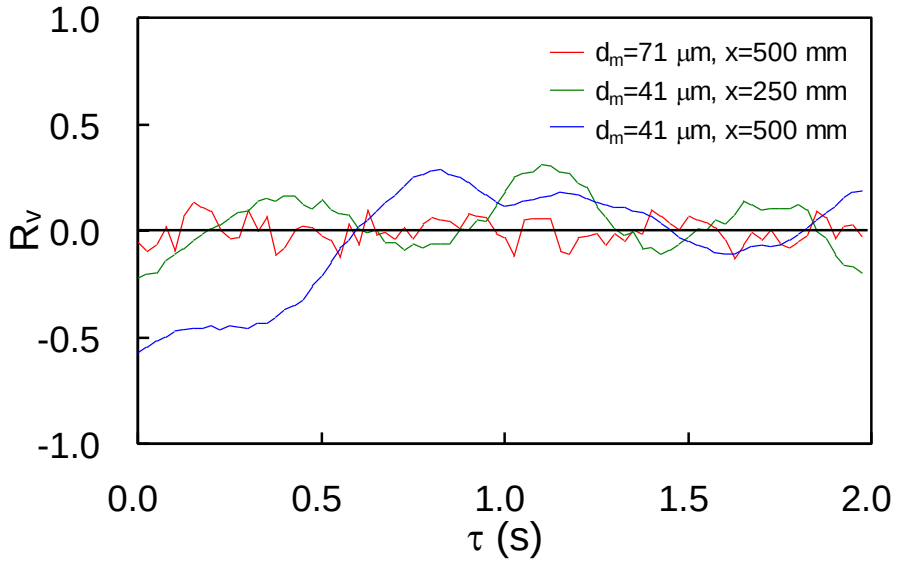

Fig. 16. Cross-correlation between L_a' and v_a'.

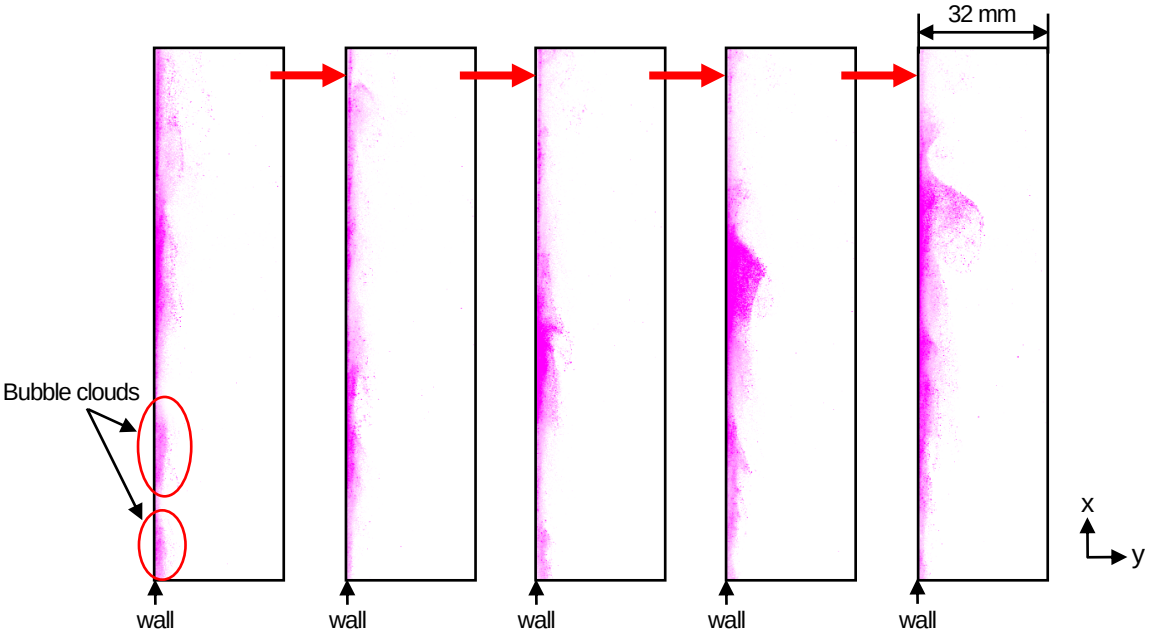

(a) t=0.0 s (b) t=0.4 s (c) t=0.8 s (d) t=1.2 s (e) t=1.6 s

Fig. 17. Typical time-series of images of bubbles near the wall for d_m=41 μm at x=500 mm.

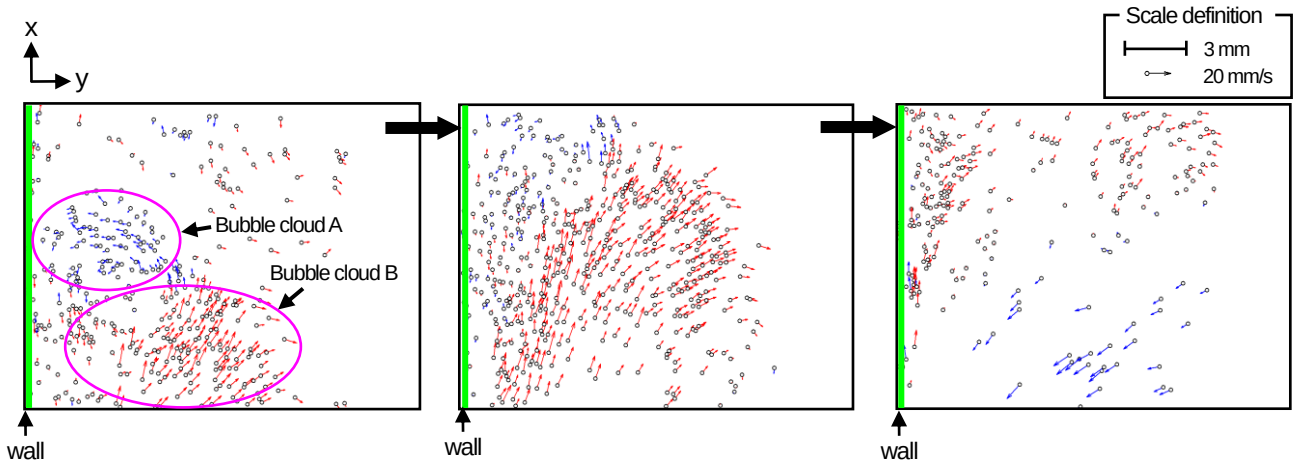

(a) t_b=0.0 s (b) t_b=0.25 s (c) t_b=0.75 s

Fig. 18. Temporal changes in bubble fluctuation velocity vector map at x=500 mm.

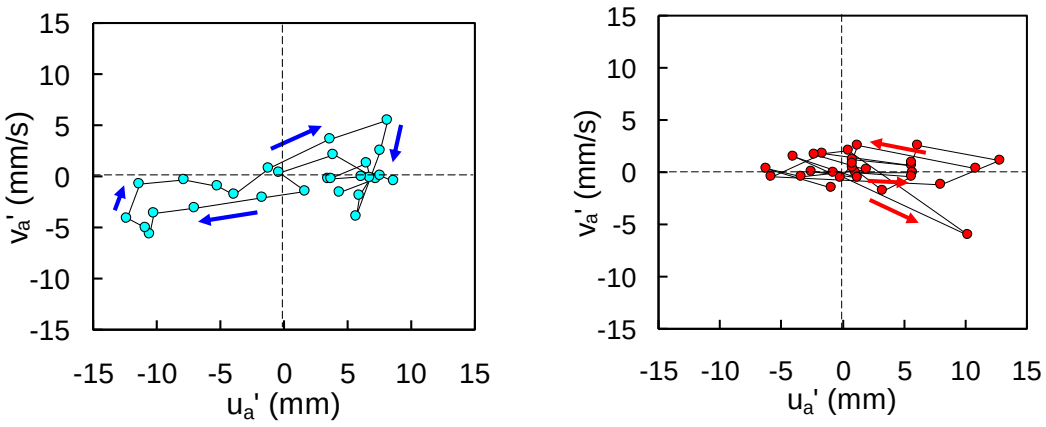

(a) d_m= 41 μm (b) d_m= 71 μm

Fig. 19. Distributions of u_a' and v_a' obtained using Figs. 12 and 15.

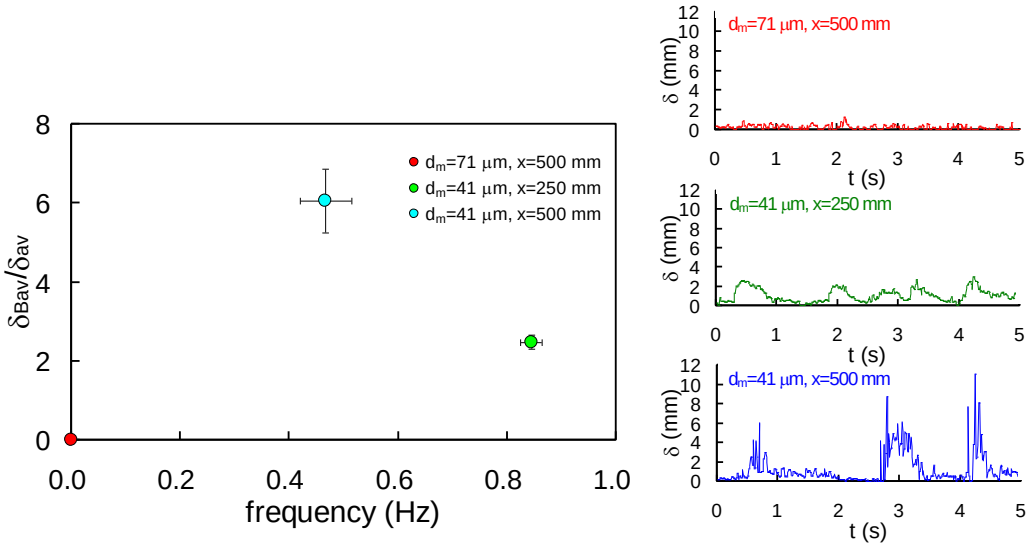

Fig. 20. Relationship between large bubble cloud formation frequency and δ_{Bav}/δ_{av}.

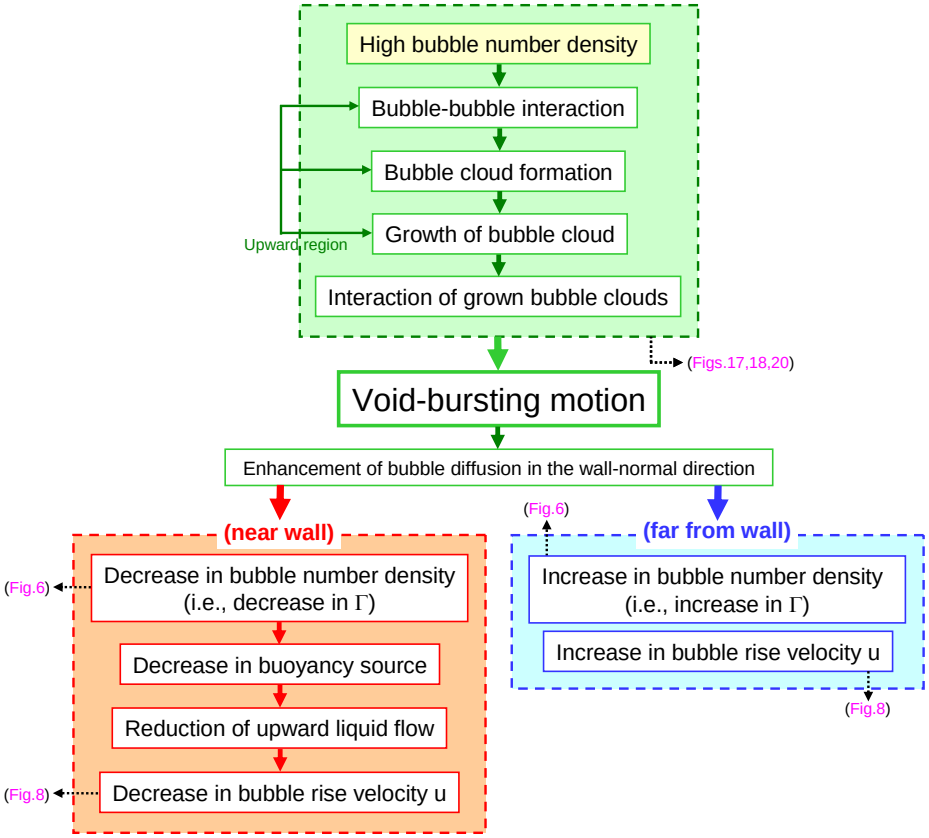

Fig. 21. Summary of void-bursting motion generation mechanism and effects of this motion on Γ and u.

Supporting information

The details of the numerical simulation method used to calculate the laminar natural convection without bubbles are explained in the following.

1. Assumptions

The main assumptions made in the numerical simulation are as follows: (1) The flow is a two-dimensional laminar flow. (2) The density is constant in the governing equations described in the following, except for that used in the buoyancy term (i.e., the Boussinesq approximation).

2. Governing equations

(1) Conservation equation for the liquid mass:

$$\nabla \cdot \mathbf{u}_{\mathrm{L}} = 0, \tag{A1}$$

where **u** is the velocity vector, and the subscript L denotes the liquid.
(2) Conservation equation for the liquid momentum:

$$\frac{\partial \mathbf{u}_{\mathrm{L}}}{\partial t} + (\mathbf{u}_{\mathrm{L}} \cdot \nabla)\mathbf{u}_{\mathrm{L}} = -\frac{1}{\rho_{\mathrm{L}}} \nabla p'_{\mathrm{L}} + \nu_{\mathrm{L}} \nabla^2 \mathbf{u}_{\mathrm{L}} + \beta_{\mathrm{L}} g(T_{\mathrm{L}} - T_{\mathrm{L},\infty})\mathbf{i}_{\mathrm{x}}, \tag{A2}$$

where ρ is the density, p' is the fluctuating pressure, ν is the kinematic viscosity, β is the coefficient of volume expansion, T is the temperature, $\mathbf{i}_{\mathrm{x}}$ is the unit vector in the streamwise direction, and the subscript ∞ denotes the ambient condition. The third term on the right-hand side is the buoyancy force induced by the density difference in the liquid.
(3) Conservation equation for the liquid energy:

$$\frac{\partial T_{\mathrm{L}}}{\partial t} + (\mathbf{u}_{\mathrm{L}} \cdot \nabla)T_{\mathrm{L}} = \alpha_{\mathrm{L}} \nabla^2 T_{\mathrm{L}}, \tag{A3}$$

where α is the thermal diffusivity.

A simplified marker-and-cell (SMAC) method is used for the pressure-velocity coupling. The governing equations are discretized using the finite differential method and all the spatial derivative terms in Eqs. (A1)–(A3) are discretized using a staggered grid system. A two-dimensional cubic interpolated propagation (CIP) scheme, which was proposed by Takewaki and Yabe [1], is applied to the advection terms in Eqs. (A2) and (A3). The viscous term in Eq. (A2) and the thermal conductivity term in Eq. (A3) are discretized in space using a second-order central difference scheme.

3. Computational domain

The *x* and *y* axes are set along the streamwise and wall-normal directions, and have zeros at the bottom of the tank and at the center of the inside wall, respectively. The lengths of the computational domains in the *x* and *y* directions are set at 1630 mm and 270 mm, respectively, by considering the sizes of both the container and the bubble generator used in the experiments. The heating region under uniform heat flux conditions is set to be

x=130−965 mm. Non-slip conditions are imposed on the bottom and on both sidewalls of the computational domain. In contrast, a free-slip condition with a constant temperature (22 ˚C) is imposed on the top of the computational domain to express the gas-liquid interface. The grid intervals in both the x and y directions are 1 mm.

References

Takewaki, H., Yabe, T., 1987. The cubic-interpolated pseudo particle (CIP) method: application to nonlinear and multi-dimensional hyperbolic equations. Journal of Computational Physics 70, 355-362.